Effect of contact alignment on shrinkage anisotropy during sintering: Stereological model, discrete element model and experiments on NdFeB compacts

Brice Hugonnet, Jean-Michel Missiaen, Christophe Martin, Cyril Rado

Materials and Design 191 (2020) 108575

Contents lists available at ScienceDirect

Materials and Design

journal homepage: www.elsevier.com/locate/matdes

Effect of contact alignment on shrinkage anisotropy during sintering: Stereological model, discrete element model and experiments on NdFeB compacts.

B. Hugonnet [b], J.-M. Missiaen [a,*], C.L. Martin [a], C. Rado [b]

[a] Université Grenoble Alpes, CNRS, Grenoble INP, SIMAP, 38000 Grenoble, France
[b] CEA, LITEN, F-38054 Grenoble, France

HIGHLIGHTS

- Synthesis of the different sources of shrinkage anisotropy during sintering from the literature
- Quantitative link between the shrinkage anisotropy factor and the distribution of particle contact orientations
- Three approaches are compared: a stereological model; a discrete element method; results on NdFeB magnetic powder compacts.

GRAPHICAL ABSTRACT

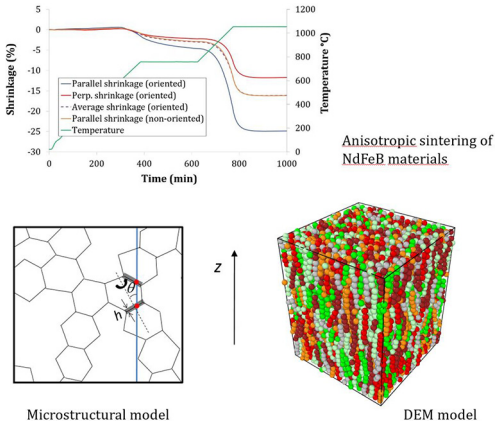

ARTICLE INFO

Article history:
Received 28 October 2019
Received in revised form 16 February 2020
Accepted 17 February 2020
Available online 24 February 2020

Keywords:
Anisotropy
Contacts
NdFeB
Shrinkage
Sintering

ABSTRACT

This works aims at analysing the effect of alignment of particle contacts on the shrinkage anisotropy during sintering. A stereological model is proposed which relates the shrinkage anisotropy factor to the distribution of contact area orientations. The shrinkage anisotropy is further analysed by using a discrete element method (DEM) to simulate the sintering of isostatically compacted packings of aligned particle chains. Finally, the analysis is performed on experimental magnetically oriented NdFeB powder compacts. The stereological model predicts a higher shrinkage in the direction of preferentially aligned contacts, in agreement with DEM simulations and experimental results, where a shrinkage anisotropy factor close to 2 is observed.

* Corresponding author.
E-mail address: jean-michel.missiaen@simap.grenoble-inp.fr (J.-M. Missiaen).

https://doi.org/10.1016/j.matdes.2020.108575

1. Introduction

Most powder processes are intrinsically anisotropic, with preferential directions related to the compaction or casting process and to the part geometry. The green body resulting from the powder forming step may exhibit different kinds of microstructural anisotropy: (1) anisotropy of the particle packing (2) anisotropy of particle orientations (3) anisotropy of the orientation, number, morphology or crystallography of contacts. Microstructural anisotropy is usually responsible for anisotropic shrinkage during free sintering of a green part. This is an important issue in materials design since it may cause distortions of the part and prevent net-shape processing, which is one of the main advantages of powder metallurgy. In case of multi-layer ceramics, it can even be responsible for delamination or warpage [1]. A shrinkage anisotropy factor k can be introduced, which quantifies the ratio between the shrinkage parallel ($\varepsilon_{//}$) and perpendicular ($\varepsilon_{\perp}$) to a preferential orientation axis in the microstructure:

$$k = \frac{\varepsilon_{//}}{\varepsilon_{\perp}} \quad (1)$$

The difficulty to give a quantitative prediction of shrinkage anisotropy during sintering or even to predict the direction of shrinkage anisotropy in practical situations is related to the multiple microstructural features of the green body anisotropy resulting from the powder forming process. These different sources of anisotropy may combine, each with different intensities and possibly in different directions, to produce the observed shrinkage anisotropy. These aspects, however, are rarely addressed in the literature in a synthetic way. In the following, the main sources of microstructural anisotropy and their respective effect on shrinkage anisotropy are discussed from literature results, in relation with powder forming. This analysis is summarized in Table 1.

Table 1
Summary of the main sources of microstructural anisotropy and their effect on shrinkage anisotropy, in relation with powder processing.

		Microstructural anisotropy				
		Morphological texture ***(platelike particles, rods)***	Anisotropic contact numbers ***(isometric grains)***	Contact flattening ***(ductile materials)***	Crystallographic texture ***(isometric grains)***	Porous layers
	z ↑		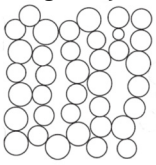	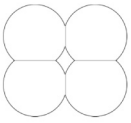	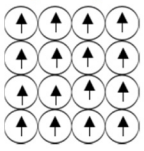	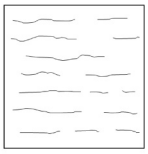
	Preferential orientation	Platelike particles aligned $\perp$ z (or rods $\perp$ z and y in tape casting)	More contacts // z	Contacts flattening $\perp$ z	Crystallographic axis $\vec{c}$ // z	Porous layers $\perp$ z
Powder processing	Uniaxial compaction	Higher shrinkage // z [2, 8]	Lower shrinkage // z [27] or higher shrinkage // z [28, this work]	Higher shrinkage $\perp$ z [2, 3]	-	Higher shrinkage // z [14]
	Tape casting	Higher shrinkage // y and z [7, 11]	-	-	-	-
	Injection moulding	Higher shrinkage $\perp$ z near the walls [5, 6, 9], or // z in the center [5, 9]	-	-	-	-
	Alignment under high magnetic field	Higher shrinkage // z [4, 10]	Higher shrinkage // z [28, this work]	-	Higher shrinkage // z [10, 16, 21-26, this work]	-
	3D-printing	-	-	-	-	Higher shrinkage // z [15]

z = direction of compaction, of the magnetic field, of the paste flow (powder injection moulding), of the normal to the film (tape casting), building direction (3D-printing).
x = casting direction (tape casting).
y = direction perpendicular to the casting direction in the casting plane (tape casting).

An important source of anisotropy during uniaxial compaction of metallic powders is the plastic deformation of contacts which may be larger in the direction of pressure application. From simple geometrical arguments, mass transport to the pores will be slower for larger contacts and shrinkage will then be greater in the transverse direction, at least in a first step. Zavaliangos and Bouvard [2] confirmed this point by simulations with initially isometric particles. Contact flattening may also decrease the compact compliance in the direction of pressure application, which would again facilitate particle rearrangement and shrinkage in the transverse direction. Discrete element simulations that take into account this effect also confirm that shrinkage following uniaxial compaction is initially larger in the transverse direction [3].

Anisotropy due to preferential orientation of anisometric particles (morphological texture), as induced for example by tape casting, is one of the most reported source of sintering anisotropy for ceramic particles [4–10]. Anisotropic shrinkage in this case is often explained by the shorter average spacing between interparticle contacts in the direction perpendicular to the plane of alignment, for plate-like particles. This interpretation is too simplistic since the morphology of the pore surface and especially the curvature at the grain boundary tip in both directions is not the same, which may influence mass transport kinetics. However, 2D simulations of the shrinkage of oriented ellipsoïdal particles, which take into account the pore curvature, confirm that this intuitive interpretation is correct and that shrinkage is greater perpendicular to the direction(s) of particle alignment, except in the last stage of sintering where this trend can be reversed [11–13].

Defects created in the forming step may also be responsible for a shrinkage anisotropy. For example, aligned elongated pores can be formed during compact ejection or debinding after uniaxial compaction [14]. Large porous areas can also remain between the printed layers in 3D-printing [15]. This usually results in a higher shrinkage during the first stages of sintering in the direction perpendicular to the porous layers, where particle rearrangement is facilitated [14,15]. Shrinkage anisotropy then decreases during the late stage of sintering, as the pores tend to spheroidize after closing.

Crystallographic texture is another possible source of shrinkage anisotropy [16]. Indeed, orientation of plate-like particles in tape-casting is related to a crystallographic texture [17,18], which may influence the anisotropic behaviour during sintering, in addition to the effect of the morphological texture already discussed. A crystallographic texture can also be created with isometric particle by aligning particles in high magnetic field before filter-pressing, uniaxial compaction or injection moulding [4,19–22]. A strong crystallographic texture is thus created in the green body while the morphological texture can hardly be detected initially. The sintering shrinkage is then generally larger along the direction of field application, with a shrinkage anisotropy factor usually between 1.5 and 2 for hexagonal ferrites or NdFeB hard magnetic particles [23–26]. Such a large effect is difficult to explain. Zavaliangos et al. [16] obtained a larger shrinkage along the direction of field application using finite element method (FEM) simulations, assuming a lower energy for grain boundaries perpendicular to that direction. However, the predicted shrinkage anisotropy factor was smaller and anisotropy in atomic diffusivities may further complicate the analysis.

The anisotropic distribution of interparticle contacts may also be a source of shrinkage anisotropy. This effect often accompanies the deformation of contacts in uniaxial compaction or the preferential orientation of anisometric particles in tape casting, whose specific effects were discussed above. However, this may be the main source of anisotropy in the case of compacting hard and isometric particles, for which the plastic deformation and orientation of particles may be neglected. Shima and Saleh [27] observed a higher shrinkage during sintering in the direction where the stress was smaller during compaction of ceramic isometric particles, and explained it by a higher compliance of the packing in that direction, due to the smaller number of contacts. However they did not quantify the anisotropy in contact numbers and he did not discuss the effect of the sintering stress which should also depend on the contact number and may compensate for the difference in compliance. In contrast, Tanaka et al. [28] observed a 15% higher shrinkage in the compaction direction for powder compacts obtained by uniaxial compaction of isometric ceramic particles. They could relate this anisotropy to a higher number of contacts in a similar proportion along the compaction direction, as quantified by an optical method. Also in directional freeze casting, elongated macropores may induce a slightly higher shrinkage in the casting direction, which was related to the slightly lower number of particle contacts in the transverse direction [29]. Anisotropic sintering was also observed for colloidal processing of ceramic particles under a magnetic field, with a higher shrinkage in the direction of apparent contact alignment [30].

In this work, a quantitative analysis of the link between the shrinkage anisotropy factor and the distribution of particle contact orientations in a powder compact is proposed for the first time. The geometry, chemistry, crystallography of contacts is assumed uniform, so that everything but the contact number has an isotropic uniform distribution. This situation can be met during sintering of uniaxially compacted isometric ceramic particles. It is also representative of magnetic hard particles which are formed by uniaxial compaction, powder injection moulding or filter pressing in high magnetic field.

In a first section, we propose a stereological approach to quantify the shrinkage anisotropy factor in the case of an anisotropic distribution of contact numbers. The ratio between the shrinkage parallel and perpendicular to the preferential orientation is computed as a function of the anisotropy in particle contact numbers. In a second part, discrete element simulations are used to calculate this shrinkage anisotropy factor for an anisotropic particle packing. Finally, sintering experiments on NdFeB magnetic powder compacts oriented in a high magnetic field are analysed. The 3D distribution of contact orientations is reconstructed from image analysis measurements on material cross sections. The shrinkage anisotropy factor is deduced from dilatometric measurements in the direction parallel and perpendicular to the direction of preferential orientation. Results of the experiments and models are discussed and conclusions are drawn regarding the effect of an anisotropic distribution of contacts on the shrinkage anisotropy.

2. Stereological model

Let us consider a powder compact with isometric particles. The microstructural anisotropy is assumed to simply result from a preferential alignment of particle contacts along the vertical axis *z*. For sake of simplicity, an axisymmetric distribution of the contact normals around axis *z* is assumed (Fig. 1). Particle contacts are supposed uniform throughout the compact (similar neck size, surface curvature, surface and grain boundary energy, …), and mechanical interactions induced

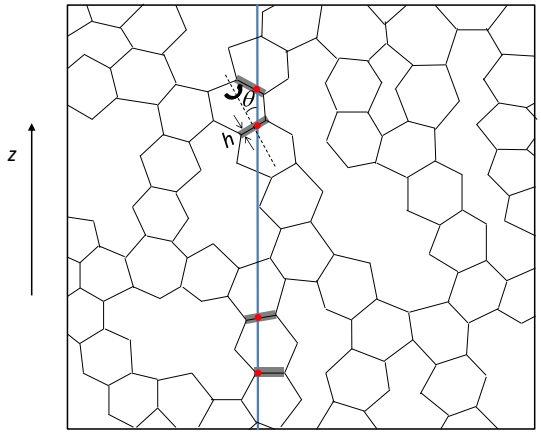

Fig. 1. Illustration of the relation between macroscopic shrinkage and the distribution of contact normal orientations.

by packing heterogeneity are neglected, so that indentation h may be assumed to be the same for all contacts at a given sintering state (as quantified by the volumetric shrinkage ε_V). The proposed model describes the effect of an anisotropy in contact numbers on the shrinkage anisotropy, other things being equal. It simply computes the shrinkage anisotropy factor k (Eq. (1)) between the direction of contact alignment z and the direction perpendicular to z. In case of variation of the contact anisotropy during sintering, the model can still be applied to predict the instantaneous shrinkage rate ratio as a function of microstructural parameters.

Orientations are referenced in spherical coordinates with respect to the preferential axis of alignment z. θ is the angle between the contact normal and the z axis, and φ the azimuthal angle. The elementary solid angle $d\Omega\,(\theta,\varphi)$ is equal to $\sin\theta\, d\theta\, d\varphi$ (Fig. 2).

Let $s_V(\theta)$ denote the surface area of contact (grain boundary area) per unit volume and per unit solid angle, with normal oriented along θ with respect to z, and $N(\theta)$ the number of such contact per unit solid angle. Let us consider a random straight line which cross the powder compact along direction z (Fig. 1). The line intersects $N(\theta)\, d\Omega\,(\theta,\varphi)$ contacts with normal in the solid angle $d\Omega\,(\theta,\varphi)$. With the above assumptions, the length reduction ΔL due to sintering of such contacts is simply equal to $N(\theta)\, d\Omega\,(\theta,\varphi)\, h \cos\theta$. The macroscopic shrinkage $\varepsilon_z(\theta)$ along direction z can then be related to the corresponding number of contact per unit length $N_L(\theta)\, d\Omega\,(\theta,\varphi)$ in the direction z:

$$\varepsilon_z(\theta) = (\Delta L/L)_z(\theta) = N_L(\theta)\, d\Omega\,(\theta,\varphi)\, h\, \cos\theta \tag{2}$$

Furthermore, stereology tells us that the average number of contacts intersected per unit length along z is equal to the surface area of contact per unit volume projected on a plane perpendicular to z [31]:

$$N_L(\theta)\, d\Omega\,(\theta,\varphi) = s_V(\theta)\, d\Omega\,(\theta,\varphi)\, \cos\theta = s_V(\theta)\, \cos\theta\, \sin\theta\, d\theta\, d\varphi \tag{3}$$

The total shrinkage ε_z along direction z is then obtained from Eqs. (2) and (3) by summing on all solid angles:

$$\begin{aligned}\varepsilon_z &= \int_0^{2\pi} d\varphi \int_0^{\frac{\pi}{2}} s_V(\theta)\, h\ \cos^2\theta\ \sin\theta\, d\theta \\ &= 2\pi\, h \int_0^{\frac{\pi}{2}} s_V(\theta)\ \cos^2\theta\ \sin\theta\, d\theta\end{aligned} \tag{4}$$

The same calculation can be performed in a direction perpendicular to z, by replacing the projected indentation by $h \sin\theta \cos\varphi$, and the projected surface area per unit volume on a perpendicular plane by $s_V(\theta) \sin\theta \cos\varphi$, for each normal oriented in the solid angle $d\Omega\,(\theta,\varphi)$. The global transverse shrinkage $\varepsilon_\perp$ is obtained by summing on all solid angles:

$$\begin{aligned}\varepsilon_\perp &= \int_0^{2\pi} \cos^2\varphi d\varphi \int_0^{\frac{\pi}{2}} s_V(\theta)\, h\ \sin^2\theta\ \sin\theta\, d\theta \\ &= \pi\, h \int_0^{\frac{\pi}{2}} s_V(\theta)\ \sin^2\theta\ \sin\theta\, d\theta\end{aligned} \tag{5}$$

In case of a preferential alignment of the contacts perpendicular to z, $s_V(\theta)$ is larger for values of θ close to 0 and ponderation by $\cos^2\theta$ or $\sin^2\theta$ in Eqs. (4) and (5) will induce a larger shrinkage in the direction parallel to z.

Quantification of the shrinkage (or shrinkage rate) anisotropy needs the distributions of contact orientations to be specified. Let us first assume an isotropic distribution, S_V being the specific surface area of contacts, *i.e.* the total surface area per unit volume. The surface area per unit solid angle is then simply:

$$s_V(\theta) = \frac{S_V}{2\pi} \tag{6}$$

Shrinkage in the direction parallel and perpendicular to z is then easily calculated by introducing this expression in Eqs. (4) and (5):

$$\varepsilon_z = \varepsilon_\perp = \frac{1}{3} h\, S_V \tag{7}$$

Shrinkage is then isotropic, as expected, and the volumetric shrinkage can be deduced:

$$\varepsilon_V = \left(\frac{\Delta V}{V}\right) = \varepsilon_z + 2\varepsilon_\perp = h\, S_V \tag{8}$$

which is nothing but the expression of volume conservation, since both expressions represent the volume of matter per unit volume transferred to the pores.

If we now consider an anisotropic orientation of contacts, the volumetric shrinkage is written from Eqs. (4) and (5):

$$\varepsilon_V = \varepsilon_z + 2\varepsilon_\perp = 2\pi\, h \int_0^{\frac{\pi}{2}} s_V(\theta)\ \ \sin\theta\, d\theta = h\, S_V \tag{9}$$

The average shrinkage is thus equal to the shrinkage of an isotropic system with the same specific surface area of contacts. This is a consequence of the assumption of identical contacts in the model, since the anisotropic system differs from the isotropic one simply by the distribution of contact orientations.

The shrinkage anisotropy factor can be expressed from Eqs. (4) and (5):

$$k = \frac{\varepsilon_z}{\varepsilon_\perp} = \frac{2\int_0^{\frac{\pi}{2}} s_V(\theta)\ \cos^2\theta\ \sin\theta\, d\theta}{\int_0^{\frac{\pi}{2}} s_V(\theta)\ \sin^2\theta\ \sin\theta\, d\theta} \tag{10}$$

Assuming an axisymmetric distribution of the contact normals around the z axis:

$$s_V(\theta) = S_V\, f(\theta) \tag{11}$$

where the distribution density $f(\theta)$ per unit solid angle can be modelled

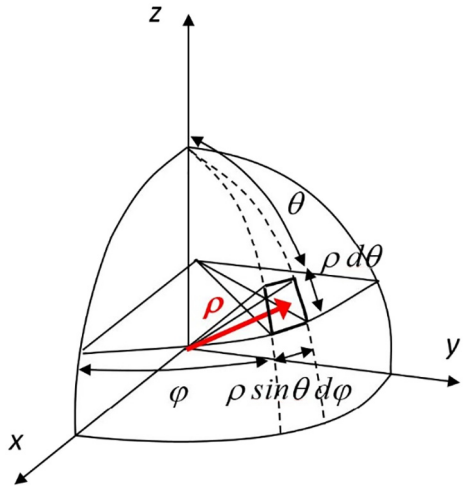

Fig. 2. Representation of a contact normal with the elementary solid angle in spherical coordinates.

by a March-Dollase function, as in Ref. [32, 33]:

$$f(\theta) = \frac{1}{2\pi}\left(r^2\cos^2\theta + \frac{1}{r}\sin^2\theta\right)^{-3/2} \quad (12)$$

The anisotropy can be adjusted by varying the function parameter r between $r = 0$ for particles perfectly aligned along the z axis and $r = 1$ for a uniform isotropic distribution of contact orientations. Fig. 3 presents the distribution for 3 different values of parameter r. The shrinkage anisotropy factor k was computed numerically using Eqs. (10)–(12), for any value of r. Fig. 4 gives the variation of k with the parameter r of the March-Dollase distribution, deduced from the stereological model. The same result would be obtained for the shrinkage rate anisotropy factor.

3. Discrete element model

The Discrete Element Method (DEM) is used to simulate the sintering of aligned particle chains. Our in-house code, dp3D, is used both for the preparation of the compact by isostatic compaction and for its sintering. The details of the simulation methodology and of the sintering model can be found in earlier publications [3,34,35]. Only the main aspects will be reported here. The powder compact is modelled as an assembly of spherical particles interacting through their contacts. The total force (sum of all contact forces) applied on each particle is computed and a dynamic scheme updates the new position of particles using the second law of motion at each time step. New contacts or contact losses are updated at each time step.

The initial packing of particles is isostatically compacted with interaction forces that are elastic.

The normal contact force model that describes the sintering of particles is derived from the work of Parhami and McMeeking [36] and from the calculations of Bouvard and McMeeking [37] and Pan et al. [38]. The model considers grain boundary and surface diffusion to be the major mechanisms for mass transport. The input parameters of the model are the surface energy, the dihedral angle, and the grain-boundary diffusion coefficient (with its activation energy). The growth of a sintering contact between two particles is given by a generalization of Coble's law [39]. Coarsening is not included in the simulations.

Particle chains observed experimentally (see Fig. 12a, b and c) are represented in DEM by rows of spheres (see Fig. 5a). Three particle chains were tested with 4, 6 and 10 spheres. These chains are generated by randomly setting spheres in a cylinder 20% larger in radius than the spheres radius R ($2R = 5$ μm) to avoid fully straight particle chains. Fully straight chains have also been tested, but we have observed that they arrange in an ordered manner during compaction, which is not realistic. The preparation procedure for the packing of particle chains before sintering consists of three main steps. Initially, the chains are set randomly without any contact with each other in a periodic box with their principal axis oriented in the z direction (gas of particles, Fig. 5b). The spheres are bonded together elastically with high stiffness and are jammed together to attain a packing relative density D of 0.39. A total of 12,000 spheres were used to model the packing of particle chains. The procedure for jamming particles and the elastic model for bonds have been detailed elsewhere [40,41]. The Young's modulus of particles is set to 180 GPa and the radius of bonds between spheres is set to $0.3R$ to ensure a large stiffness of the elongated particles. The jammed density may be seen as similar to the tap density defined by practitioners. An isostatic compaction is then imposed on the packing, thus allowing the packing density to be increased to a value typical of the green density obtained experimentally ($D = 0.55$). The isostatic pressure is 150 MPa as in the experimental procedure. Whatever the length of the particle chains (4, 6 or 10 spheres), approximately the same anisotropic densification was obtained, with negligible shrinkage in the z direction (*i.e.* the densification is only due to radial rearrangements and deformation of particle chains). Thus, DEM simulations indicate that the anisotropic nature of the particle chains already leads to an anisotropic densification during isostatic compaction. This anisotropic densification comes with a decrease in contact orientation anisotropy as described below. Analyses of packings obtained with particle chains of different lengths (4, 6 and 10) give the same trends and only the results for the 6-particles chains will be discussed in the following.

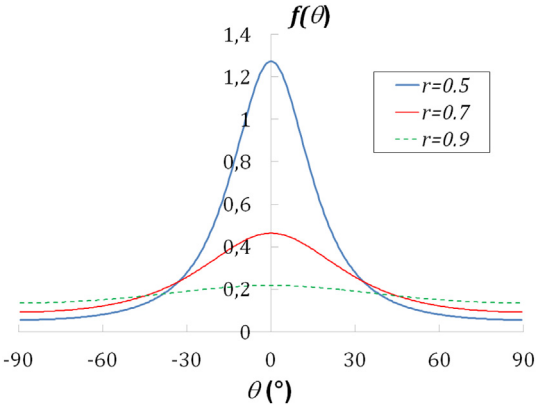

Fig. 3. Representation of the March-Dollase distribution of the specific surface area per unit solid angle, for 3 values of parameter r: $r = 0.5$; $r = 0.7$; $r = 0.9$.

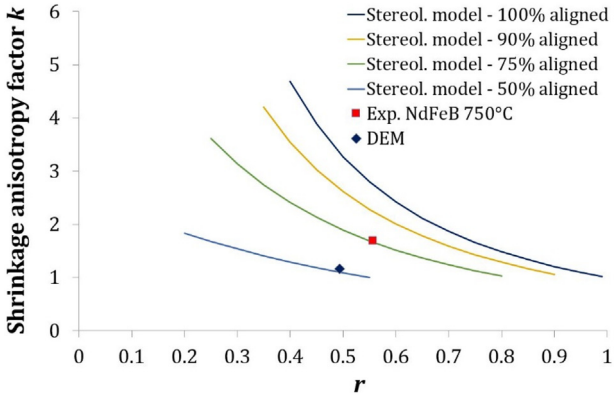

Fig. 4. Variation of the shrinkage anisotropy factor k predicted from the stereological model for an axisymmetric distribution of the contact normals with parameter r of the March-Dollase distribution (from Eq. (10), 100% aligned) and for bimodal distributions with various fractions $f_{//}$ of aligned particles ($\theta_0 = 90°$, $\sigma = 29°$, see next section, Eqs. (13) and (14)). Predictions from actual distributions of contacts of a DEM model and deduced from image analysis of a NdFeB material are also reported on the graph (see Table 2).

Fig. 6 presents the distribution of contact orientations calculated as a fraction of contacts per unit solid angle, whose normal is in a given orientation class. The contact anisotropy is significantly reduced during the isostatic compaction step (Fig. 6a and b). Lateral contacts between particle chains are created during this step, which increases the fraction of contacts oriented between 45 and 90° with respect to the anisotropy axis.

a) after jamming (relative density $D = 0.39$) b) after isostatic compaction (relative density $D = 0.55$) c) after sintering (relative density $D = 0.90$).

Fig. 7 gives the shrinkage and shrinkage rate anisotropy factors deduced from measurements of the packing dimensions in the 3 directions. The values cannot be determined precisely at the very beginning and at the very end of sintering, due to the too small shrinkage rates values. However, after initial fluctuations, the shrinkage rate anisotropy factor together with the shrinkage anisotropy factor tend to a more or less constant value of 1.4, which can be considered to be related to the average contact anisotropy in the initial particle packing after compaction. After reaching a maximum value, the shrinkage anisotropy factor decreases and tends to a value close to unity, which

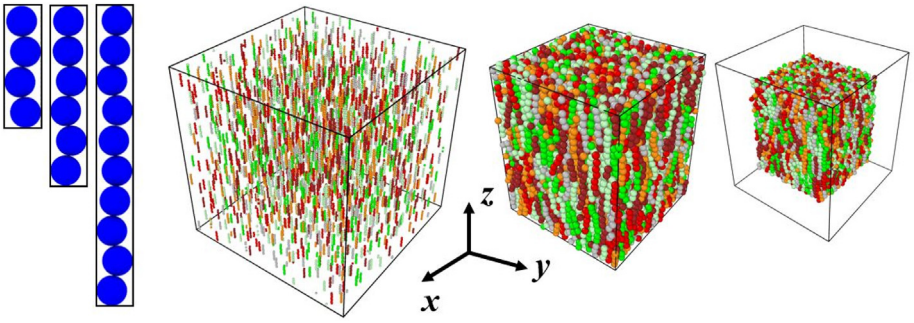

Fig. 5. a) Typical rows of spheres used to model particle chains. b) Gas of particle chains oriented in the z direction (6 spheres, $D = 0.01$). c) Green compact after jamming and isostatic compaction at 150 MPa ($D = 0.55$). Note that the periodic box is shorter in the x and y directions as isostatic compaction leads to non-isotropic densification. d) Sintered compact ($D = 0.90$). (Colour code is arbitrary and is only a guide to distinguish particle chains)

can be related to the decrease in anisotropy observed on the distribution of contact orientations (Fig. 6). In the same way as for compaction, sintering tends to decrease the anisotropy by creating more contacts in directions where they are less numerous.

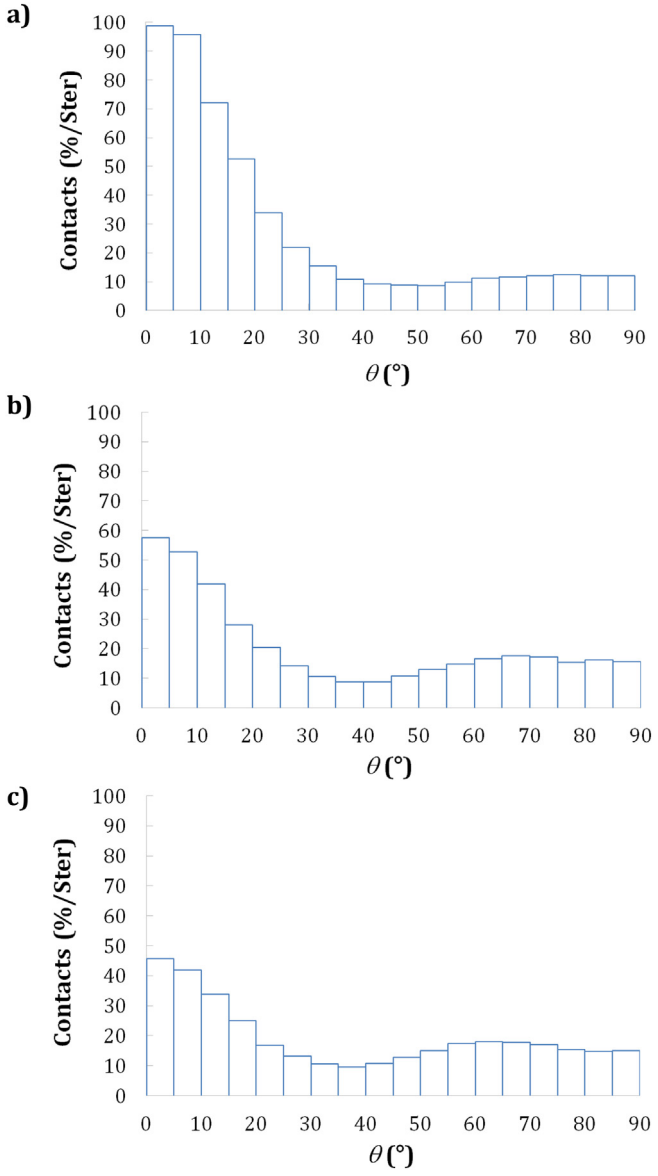

Fig. 6. Distribution of the contact normal orientations per unit solid angle with respect to the anisotropy axis z in discrete element packings.

The contact orientation distribution after compaction (Fig. 6b) cannot be described by a March-Dollase type axisymmetric distribution, due to the presence of lateral contacts. Alternatively, two populations of contacts can be considered: (i) oriented contacts with a March-Dollase type distribution density $f(\theta)$ around the z axis (Eq. (12)) and (ii) lateral contacts which have formed during compaction, which can be modelled by a normal distribution density $g(\theta)$ around θ_0 and $\pi - \theta_0$ with a standard deviation σ:

$$g(\theta) = \frac{1}{2\pi \sin\theta}\left(\frac{1}{\sigma\sqrt{2\pi}}e^{-\frac{(\theta-\theta_0)^2}{2\sigma^2}} + \frac{1}{\sigma\sqrt{2\pi}}e^{-\frac{(\theta-(\pi-\theta_0))^2}{2\sigma^2}}\right) \tag{13}$$

Assuming a fraction $f_{//}$ of oriented contacts, the bimodal distribution density of contacts per unit solid angle $f_B(\theta)$ is then expressed:

$$f_B(\theta) = f_{//}\, f(\theta) + \left(1 - f_{//}\right) g(\theta) \tag{14}$$

This distribution can be normalized as long as σ is not too large:

$$\int_0^{\frac{\pi}{2}} 2\pi \sin\theta\, f_B(\theta)\, d\theta = 1 \tag{15}$$

Fig. 8 presents the fit of the distribution of contact orientations obtained by DEM with the bimodal model of Eqs. (11)–(14). The shrinkage anisotropy factor can be computed using the stereological model from Eqs. (10)–(14) with parameters of the fit. Results are summarized in Table 2. The stereological model underestimates the shrinkage anisotropy by 15–20%. However, a slight variation of the distribution of contact orientations yields a good prediction of the shrinkage anisotropy

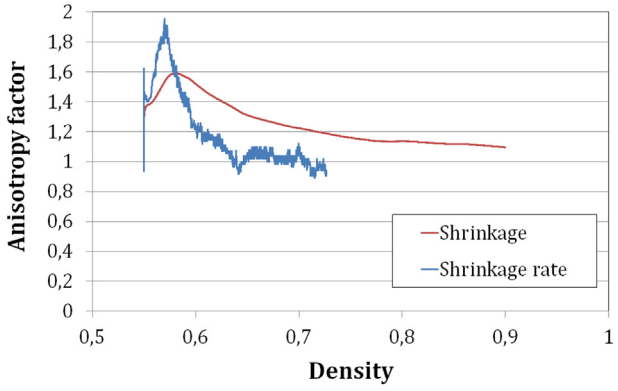

Fig. 7. Shrinkage anisotropy factor $k = 2\varepsilon_z/(\varepsilon_x + \varepsilon_y)$ and shrinkage rate anisotropy factor $k\prime = 2\varepsilon_z/(\varepsilon_x + \varepsilon_y)$ as a function of the relative density during sintering of the 6-particle chain packing compacted at $D = 0.55$.

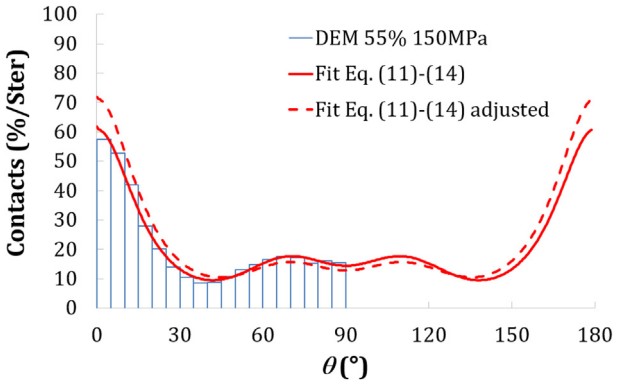

Fig. 8. Distribution of the contact normal orientations per unit solid angle with respect to the anisotropy axis z in the discrete element packing after isostatic compaction (relative density $D = 0.55$) and fit with Eqs. (11)–(14) (see Table 2 for the parameters).

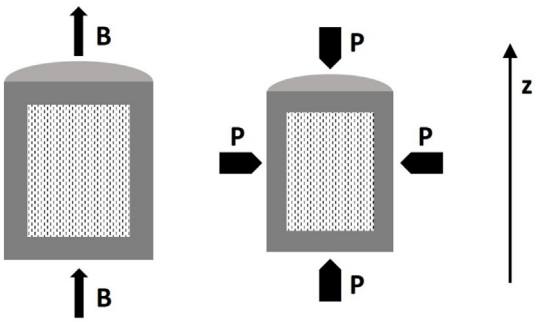

Fig. 9. Schematic representation of the powder alignment in strong magnetic field followed by isostatic compaction, and preferential orientation axis z.

factor with the stereological model (see Table 2 and Fig. 8, "adjusted"). It can be deduced that the stereological model accounts correctly for the effect of anisotropy in the orientation of contacts on shrinkage anisotropy during sintering.

4. Experiments on magnetically oriented powder compacts

Sintering experiments were performed on NdFeB hard magnetic powder compacts obtained by uniaxial compaction after orientation in high magnetic field. Strip cast ribbons of nominal composition of $Dy_{0.2}(Nd,Pr)_{13.6}Fe_{78.6}B_6(Co,Cu,Al)_{1.6}$ were used as starting material. Ribbons were decrepitated under hydrogen (HD), dehydrogenated and then turned into fine powder with a jet mill under controlled atmosphere. The granulometry of the powder is characterized by $D_{50} = 5.0$ μm, $D_{10} = 1.3$ μm and $D_{90} = 10.1$ μm and its specific surface $S_{BET} = 0.6$ m^2/g. Powder was then filled in a cylindrical silicone rubber mould and oriented parallel to the axial direction z of the cylinder using a pulsed magnetic field up to 7 T (Fig. 9). Samples were shaped in a cold isostatic press under 150 MPa to obtain a green density close to 4 g/cm^3 (relative density D ≈ 0.55). A thermal treatment consisting in a 2 °C/min temperature ramp up to a 4-hour plateau at 750 °C (to remove hydrogen induced by the powder synthesis) followed by a 2 °C/min ramp up to 1050 °C for a 4-h plateau was applied. Resulting magnets were characterized in a hysteresigraph yielding a remanence value $B_r = 1.29$ T and a coercivity value $H_c = 11.5$ kOe. The measured remanence of the sintered materials typically represents 90–92% of the calculated saturation magnetic polarization in our experimental conditions.

Dilatometric experiments were performed in a Setaram vertical differential high temperature dilatometer DHT 2050 K, with a vacuum below 6.10^{-5} mbar. Analysis was carried out in the directions parallel and perpendicular to the z axis by placing the cylindrical compact either vertical or horizontal in the dilatometer. A non-oriented sample was analysed for reference. This sample was shaped and compacted in the same conditions but without imposing a magnetic field. Fig. 10 presents the dilatometric plots of the oriented samples in directions parallel and perpendicular to the z axis and of the non-oriented powder compact. Shrinkage has been checked to be isotropic for the non-oriented sample. In contrast, a huge difference in the shrinkage parallel and perpendicular to the z axis is observed for the oriented sample, with an anisotropy factor of approximately 2 in the direction parallel to z. Shrinkage anisotropy is thus fully the consequence of orientation in the magnetic field. The average shrinkage of the oriented sample is deduced from experiments:

$$\bar{\varepsilon} = \varepsilon_z + 2\varepsilon_\perp = \frac{1}{3}\varepsilon_V \tag{16}$$

Average shrinkage of the oriented samples is at any time similar to the shrinkage of the non-oriented sample (Fig. 10). This result suggests that shrinkage anisotropy is simply related to the anisotropic distribution of contact orientations, the contact morphology being otherwise similar in the oriented and non-oriented sample.

The shrinkage anisotropy factor $k = \varepsilon_z/\varepsilon_\perp$ and the shrinkage rate anisotropy factor $k' = \dot{\varepsilon}_z/\dot{\varepsilon}_\perp$ between the direction parallel and perpendicular to the z axis are plotted as a function of sintering time on Fig. 11. After stochastic fluctuations, which are explained by the initially very low shrinkage in both directions, the value tends to 2.0 ± 0.2 for the shrinkage anisotropy factor and 2.2 ± 0.2 for the shrinkage rate anisotropy factor during the holding stage at 750 °C. These values can be considered to represent the effect of the microstructural anisotropy on the shrinkage anisotropy at the beginning of sintering in stationary conditions. A sharp increase in the shrinkage rate anisotropy factor is noticed at the beginning of the ramp following the plateau at 750 °C, due to the discontinuity in the heating cycle. This factor then decreases and tends to unity at the end of sintering, suggesting a gradual elimination of the microstructural anisotropy, as already observed for the DEM results.

Interrupted heat treatments at different temperatures were performed in a dedicated high vacuum furnace (10^{-5} mbar at 1000 °C), followed by quenching at 60 °C/min. Samples were impregnated with epoxy resin, cut along the symmetry axis z and polished to 1 μm. The microstructure was revealed using Villela's reagent as etchant. Fig. 12 shows microstructures observed in optical microscopy at different stages of sintering. The particle shape is more or less isometric. However, chain-like structures preferentially oriented along the z axis are

Table 2
Parameter of the bimodal distributions of contacts (Eqs. (12)–(14)) for the DEM materials after compaction and for NdFeB materials at the beginning of sintering ($D \approx 0.55$); shrinkage anisotropy factor k (estimation from Eq. (10) and average experimental value between shrinkage and shrinkage rate anisotropy factors).

	DEM after compaction (D ≈ 0.55)	DEM after compaction (D ≈ 0.55) adjusted	NdFeB interrupted at 750 °C (D ≈ 0.55)	NdFeB interrupted at 750 °C (D ≈ 0.55) adjusted
$f_{//}$	0.46	0.56	0.76	0.90
r	0.49	0.50	0.56	0.58
θ_0	71°	71°	89°	89°
σ	15°	15°	17°	17°
k (Eq. (10))	1.17	1.41	1.69	2.11
k (Exp.)	1.4		2.1	

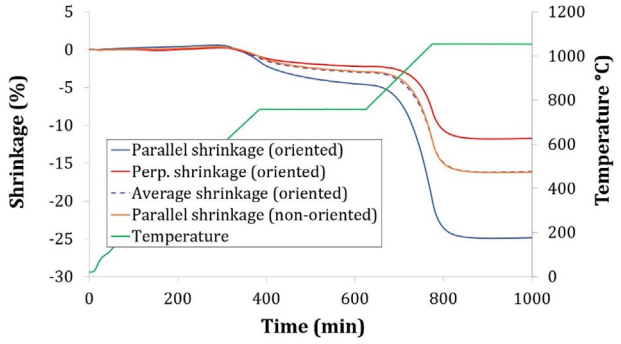

Fig. 10. Dilatometric plots of an oriented sample parallel and perpendicular to z and of a non-oriented sample (parallel to z). Average shrinkage of the oriented sample is also plotted.

observed at temperatures below 1050 °C, as the porosity is still visible. This may result from the powder process under high magnetic field, which creates particle chains due to dipolar interaction between magnetized particles [42]. Despite the high isostatic pressure applied to the sample to reach the green density, the chain-like structure is partly preserved in the powder compact. The direct consequence of this particular microstructure is a non-isotropic distribution of contacts.

Etched microstructures were analysed using Aphelion™ software. Grain separators were first reconstructed from images. For that, binary images obtained by dilation of the original image in 2 opposite directions are intersected and skeletonized with a connectivity value of 8. The operation is repeated for orientations with angle 0, π/4, π/2 and 3π/4 from the horizontal direction. Lines which separate the grains at a distance lower than 0.3 μm are thus obtained, which are assimilated to the grain boundary (GB) traces in the cross section. The 2D distribution of boundary lengths $L_2(\alpha_i)$, so-called "Rose des directions" [43], is then measured in 8 discrete directions α_i between 0 and 7π/8, by considering the corresponding local pixel configurations. The length and the weight of these local configurations are obtained as described in Ref. [44], the configurations being here simply weighted by their relative angular sectors $\frac{[\alpha_j - \alpha_{j-1} + \alpha_j}{2\alpha_j + \frac{\alpha_j + \alpha_{j+1}}{2}]}$. The distribution of length is then unbiased, as could be checked by analysis of the rose of directions on a digitized circle. The 2D distribution of grain boundary trace length can be related to the 3D distribution of the grain boundary surface area by using a stereological calculation (see Appendix A). The 2D/3D relationship was first tested with the DEM simulation by analysing 2D images on a vertical cross section of the DEM particle packing after compaction ($D = 0.55$). The same image processing was applied as with the NdFeB material to extract the grain boundaries and to measure the trace length distribution as a function of the anisotropy axis z. The experimental 2D distribution is shown on Fig. 13, together with the distribution

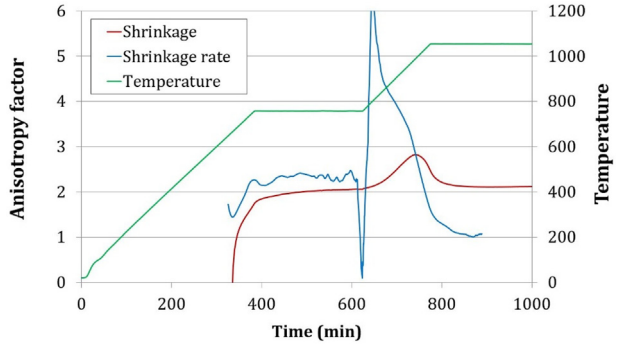

Fig. 11. Evolution of the shrinkage anisotropy factor $k = \varepsilon_z/\varepsilon_\perp$ and of the shrinkage rate anisotropy factor $k' = \varepsilon_z/\varepsilon_\perp$ with sintering time.

calculated from the 3D bimodal distribution of the grain boundary surface area (Fig. 8). The fit is fairly good, which validates the stereological relationship between 2D and 3D distributions of orientations.

The distribution of grain boundary trace lengths as a function of their orientation normal in 2D is given in Fig. 14a for the NdFeB materials sintered at 750 °C for 2 h. It confirms the preferential orientation of contacts perpendicular to the z axis. However a significant amount of contacts is also observed in the 60–90° orientation range, probably due to the formation of lateral contacts during isostatic compaction, as already observed with DEM simulations (Fig. 6a and b). The 3D distribution of GB normals which gives the best fit with the 2D distribution of GB length is then numerically determined and is plotted on Fig. 14b. Parameters of the 3D distribution are reported in Table 2.

The shrinkage anisotropy factor is calculated with the stereological model (Eq. (10)) with parameters of the GB surface area distribution deduced from the fit with 2D image analyses. A value of 1.7 is obtained, *i.e.* the model underestimates by 15–20% the experimental shrinkage anisotropy factor at the beginning of sintering, as for DEM results (Table 2). Again, a slight variation of the distribution of contact orientations yields a good prediction of the shrinkage anisotropy factor with the model (see Table 2 and Fig. 14b, "adjusted"). Agreement between the experimental shrinkage anisotropy factor and the value calculated using the stereological model of anisotropic sintering presented in the first section is fairly good, which validates that anisotropy of contact orientations is one of the main source of shrinkage anisotropy in NdFeB materials.

5. Discussion

This work presents three different analyses of the effect of contact alignment on sintering anisotropy: (i) an analytical stereological model, (ii) a discrete element simulation (DEM) and (iii) an experimental study on magnetically oriented powder compacts. From the stereological model, the shrinkage anisotropy is related to the anisotropy in contact numbers per unit length, which is a function of the anisotropy in the area of contacts (grain boundaries) orientated in the different directions. The distribution of contact areas as a function of orientation was determined experimentally on the NdFeB materials. The distribution of contact numbers as a function of orientation was obtained in DEM, which is equivalent to a distribution of contact areas for the initial packing after tapping or after compaction, since contact areas are the same for all contacts in these packings. Contact alignment also results in thermal expansion anisotropy in addition to the shrinkage anisotropy. Thermal expansion anisotropy could be analysed with our stereological model, by assuming a constant local expansion at each particle contact, as done for the constant local indentation due to sintering. However, for typical particle compacts with a relative density value D around 0.55, sintering shrinkage is about 15–20% (see Fig. 10 for the NdFeB powder compacts for example). This is much larger than thermal expansion and the effect of thermal expansion was simply neglected as a first approximation in this paper.

This work emphasizes the complexity of anisotropy in contact orientations in powder compacts. Even if particles may align preferentially in a given direction during powder forming (introduction of particle chains in DEM packings or orientation in a magnetic field in NdFeB packings), the compaction step to obtain a mechanically stable and compact packing tends to create more contacts in directions where they are initially less numerous. The resulting anisotropy in contact orientation therefore depends on the details of the powder forming step. In this work, the analysis has been restricted to initial particle packings obtained by isostatic compaction, after alignment of particle contacts along a given direction z. In both DEM and experimental NdFeB packings, the distribution of contact orientations could be described by a bimodal distribution, with an axisymmetric contribution around the preferential orientation axis z, modelled by a March-Dollase function, and a Gaussian contribution around an axis oriented between π/3 and

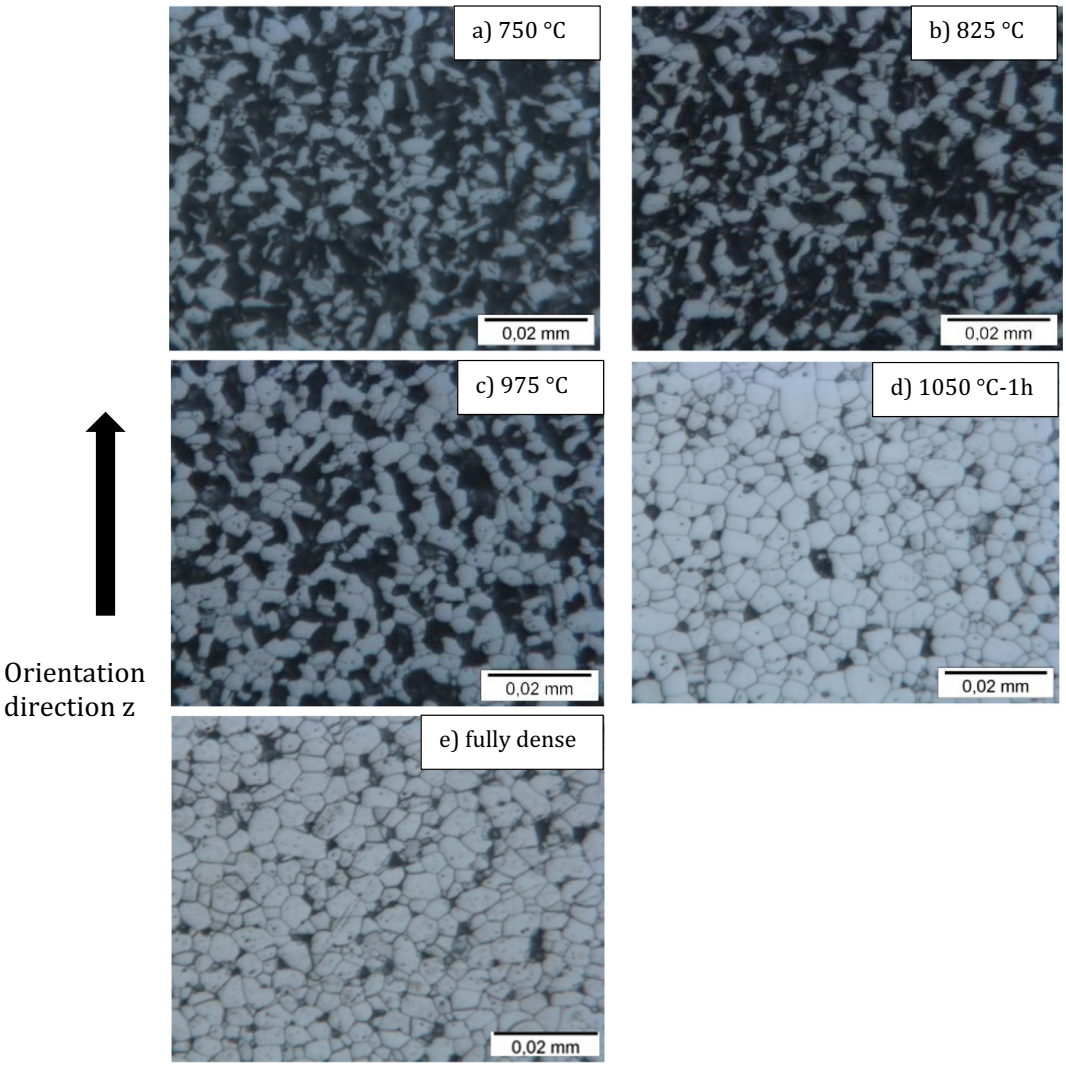

Fig. 12. Microstructure of samples after interruption at different stages of sintering.

π/2 with respect to *z*. The shrinkage anisotropy can then be computed with the stereological model using the parameters of the distribution of contact orientations in the initial packings. Both the degree of alignment, as quantified by the March-Dollase parameter *r*, and the fraction of the population of preferentially oriented contacts, $f_{//}$, control the shrinkage anisotropy factor (Fig. 4). The average value and standard deviation of the Gaussian distribution was fixed in Fig. 4 ($\theta_0 = 90°$ and $\sigma = 29°$) to analyse the effect of *r* and $f_{//}$ on the shrinkage anisotropy factor. Results of DEM and of the experimental study were also plotted on the graph, for which the fractions of aligned contacts were fitted to 0.46 (DEM) and 0.76 (NdFeB) with different values of θ_0 and σ (see Table 2), but the trend is still respected.

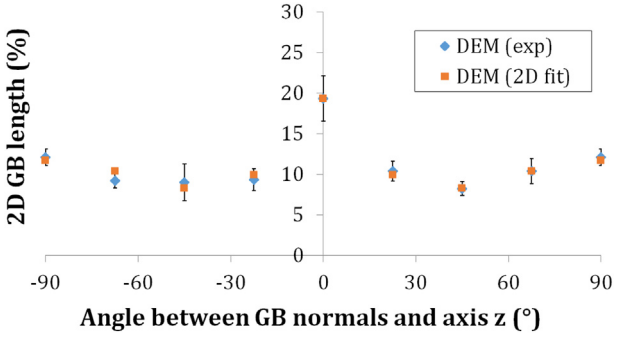

Fig. 13. 2D Distribution of GB lengths as a function of their normal orientations with respect to *z* for the DEM particle packing after compaction ($D = 0.55$): experimental results and best fit deduced from the 3D bimodal distribution of the GB surface orientations (Eqs. (11)–(14), see Fig. 8 and Table 2 for parameters) by using the stereological relationship developed in Appendix A (Eq. (24)).

Both DEM and experimental results show initially a higher shrinkage in the direction where there is a larger amount of contacts, in qualitative agreement with our stereological model and with the results of Tanaka et al. [28]. However the sintering advantage in the preferential orientation is gradually decreased as sintering proceeds. As for compaction, sintering tends to decrease the anisotropy by creating more contacts in directions where they are less numerous. These new contacts whose area is smaller than the initial contacts which have already grown will grow faster and then have a larger contribution to the shrinkage rate. Anisotropy both in contact numbers and in contact sizes then decreases throughout sintering and therefore the shrinkage anisotropy factor tends to unity at the end of sintering. Analysis of the decrease of anisotropy with densification would first need a thorough analysis of densification mechanisms, as done for example in [45], which is out of the scope of this paper.

The stereological model gives the good qualitative trend but it seems to underestimate the effect of contact anisotropy on the shrinkage anisotropy observed in DEM and in the experimental study. This is probably the limit of the analysis with a mean-field model, where contacts are assumed identical and behave the same way, without interactions. It is

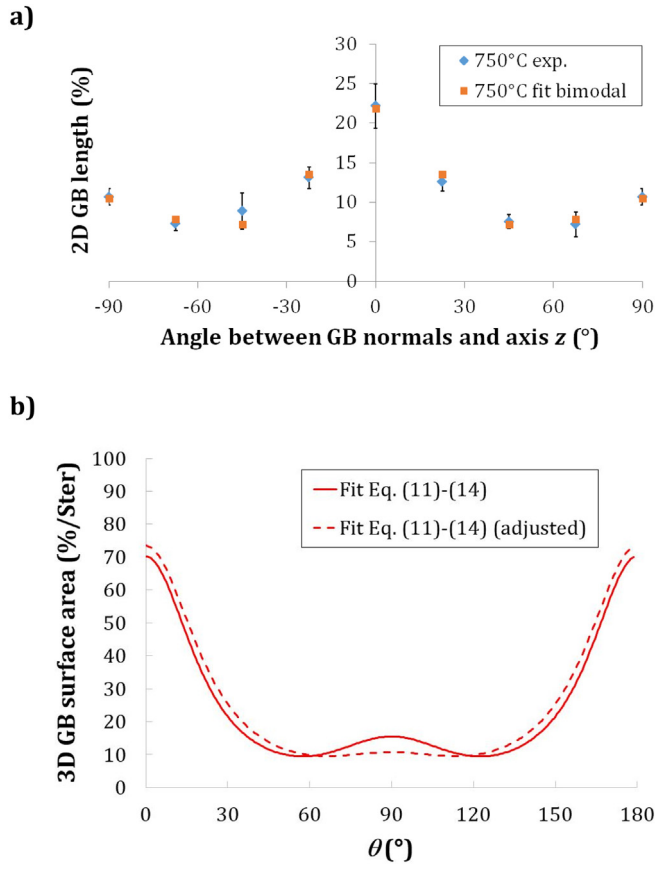

Fig. 14. a) 2D Distribution of GB lengths as a function of their normal orientations with respect to z for the NdFeB materials sintered at 750 °C for 2 h: experimental results and best fit obtained with a 3D bimodal distribution (Eqs. (11)–(14), see Table 2 for parameters) of the GB surface orientations and b) the corresponding 3D distribution of GB surface orientations (see Table 2 for the parameters).

the interest of DEM to point out this discrepancy which is then probably more related to packing effects than to intrinsic material parameters of the NdFeB system and probably depends on the initial packing conditions. For instance, particle rearrangement due to interactions between contacts or the creation of new contacts during sintering is not taken into account by the model. Other anisotropic effect may add a contribution in the case of NdFeB materials and amplify the shrinkage anisotropy: (i) slightly anisometric particles could yield a higher shrinkage perpendicular to the morphological particle alignment (Table 1), although this effect is probably limited here according to the microstructure (Fig. 12); (ii) the crystallographic texture induced by the magnetic field could enhance the growth of low energy grain boundaries perpendicular to the orientation axis (effect of dihedral angle on sintering [16]); (iii) anisotropic mass transport due to anisotropy of diffusion coefficients in the different grains boundaries, or to a non-isotropic liquid phase dispersion.

6. Conclusion

A quantitative analysis of the effect of contact alignment on sintering anisotropy is proposed for the first time by linking the shrinkage anisotropy factor to the distribution of contact orientations, first with an analytical stereological model, then with a discrete element method (DEM), finally using experimental data obtained on magnetically oriented NdFeB powder compacts, where a shrinkage anisotropy factor close to 2 was observed. From the stereological model, the shrinkage anisotropy is related to the anisotropy of contact numbers per unit length, which is a function of the anisotropy of the area of contacts (grain boundaries) orientated in the different directions. A numerical method is proposed to estimate the shrinkage anisotropy factor from the distribution of contact orientations. DEM and NdFeB particle packings build by isostatic compaction of particles previously aligned along a preferential axis both show a bimodal distribution of contact orientations, since compaction creates more contacts in directions where they are initially less numerous. In these situations, the stereological model predicts a higher shrinkage in the direction of contact alignment, but underestimates by 15–20% the sintering shrinkage anisotropy factor measured in DEM and on the experimental NdFeB materials. Experimental uncertainty in the distribution of contact orientations could explain at least part of the discrepancy, due to the high sensitivity of the shrinkage anisotropy factor to this distribution. Other effects which are not taken into account by the model may also play a role, such as particle rearrangement in general or crystallographic texture in the case of NdFeB materials. By a quantitative description of the shrinkage anisotropy due to contact alignment, this work also allows to anticipate part distortions and to improve net-shape processing in materials design.

Funding

This research did not receive any specific grant from funding agencies in the public, commercial, or not-for-profit sectors.

Data availability

The raw/processed data required to reproduce these findings cannot be shared at this time due to technical or time limitations.

CRediT authorship contribution statement

B. Hugonnet: Investigation.**J.-M. Missiaen:**Writing - original draft, Academic supervision.**C.L. Martin:**Resources.**C. Rado:**CEA supervision, Resources.

Declaration of competing interest

The authors declare that they have no known competing financial interests or personal relationships that could have appeared to influence the work reported in this paper.

Appendix A. Reconstruction of the 3D distribution of grain boundary orientations from the 2D distribution of grain boundary trace orientations

Distribution of orientations of the trace normals to the grain boundaries in 2D can be determined by image analysis in cross-sections. Reconstruction of the axisymmetric distribution of the 3-D grain boundary normals is performed as explained below.

Let us consider a 2-D section of grain boundaries in a vertical plane containing the anisotropy axis z. Let us consider an elementary trace of length dL of a grain boundary in the section plane, whose normal is oriented between ω and $\omega + d\omega$ with respect to z. The normal to the corresponding 3-D grain boundary can describe a circular band, depending on the angle β between the 2-D and 3-D normals (Fig. 15). For a given value of β, let us note θ (ω, β) the angular misorientation between the 3-D-normal and the anisotropy axis z and $s(\theta)$ the surface area of grain boundaries per unit solid angle oriented at θ with respect to the anisotropy axis. This angle can be related to ω and β from simple geometrical

considerations:

$$\theta(\omega,\beta) = acos(\ \cos\omega\ cos\beta) \tag{17}$$

The solid angle $d\Omega\ (\omega,\beta)$ for a 3D normal between β and $\beta + d\beta$ and a 2D (and 3D) normal between ω and $\omega + d\omega$ with respect to z is:

$$d\Omega(\omega,\beta) = d\omega\ \cos\beta\ d\beta \tag{18}$$

The surface area in the solid angle is then

$$ds(\omega,\beta) = s(\theta(\omega,\beta))\ \cos\beta\ d\omega\ d\beta \tag{19}$$

Let us consider a surface element dS with a 3D normal oriented at θ with respect to the anisotropy axis. Let us note dL the intersected length of the surface element with the section plane and dh the width in the other direction. The number of such surface elements in the solid angle is:

$$dN(\omega,\beta) = \frac{s(\theta(\omega,\beta)\ \cos\beta\ d\omega d\beta}{dLdh} \tag{20}$$

And the probability that such a surface element is hit by the section plane is:

$$dP(\beta) = \frac{dh\ \cos\beta}{h} \tag{21}$$

where h is the total length of the specimen.

The total length of grain boundary traces with normal between ω and $\omega + d\omega$ with respect to z is then given by:

$$L(\omega)d\omega = 2\int_0^{\pi/2} dN(\omega,\beta)\ dP(\beta)dL \tag{22}$$

where the factor of 2 accounts for the two symmetric parts of the band. Finally:

$$L(\omega)d\omega = 2\int_0^{\pi/2} s(\theta(\omega,\beta))\frac{\cos^2\beta}{h}d\omega d\beta \tag{23}$$

The specific boundary length in the plane section is then deduced:

$$L_A(\omega) = 2\int_0^{\pi/2} s_V(\theta(\omega,\beta))\ \ \cos^2\beta d\beta \tag{24}$$

There is no general solution to the problem of reconstruction of the 3-D orientation distribution $s_V\ (\theta)$ from the measured 2-D distribution $L_A(\omega)$. Here it is assumed that the 3-D distribution is axisymmetric and that it can be modelled by the March-Dollase equation (Eq. (12)). The 3-D angular orientation distribution $s_V\ (\theta)$ can then be reconstructed from the 2-D measured angular orientation distribution $L_A(\omega)$ by adjusting parameter r for a best fit between Eq. (24) and measured $L_A(\omega)$.

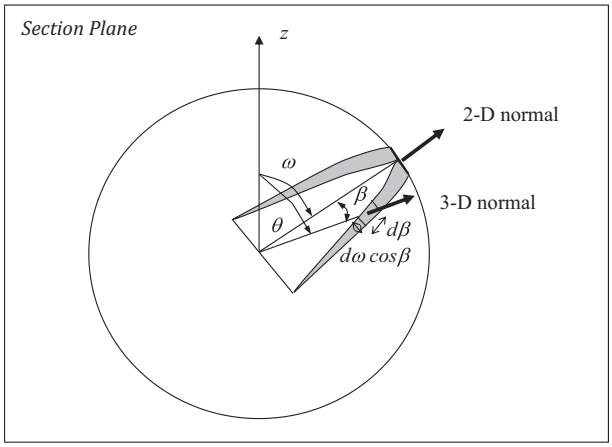

Fig. 15. Relative position of the 2-D and 3-D normals to the grain boundaries.

References

[1] M. Hagymasi, A. Roosen, R. Karmazin, O. Dernovsek, W. Haas, Constrained sintering of dielectric and ferrite LTCC tape composites, J. Eur. Cer. Soc. 25 (12) (2005) 2061–2064.
[2] A. Zavaliangos, D. Bouvard, Numerical simulation of anisotropy in sintering due to prior compaction, Int. J. Powder Metall. 36 (7) (2000) 58–65.
[3] C.L. Martin, L.C.R. Schneider, L. Olmos, D. Bouvard, Discrete element modeling of metallic powder sintering, Scripta Mater 55 (5) (2006) 425–428.
[4] J.S. Reed, R.M. Fulrath, Characterization and sintering behavior of Ba and Sr ferrites, J. Amer. Cer. Soc. 56 (4) (1973) 207–211.
[5] T. Zhang, S. Blackburn, J. Bridgwater, Debinding and sintering defects from particle orientation in ceramic injection moulding, J. Mater. Sci. 31 (22) (1996) 5891–5896.
[6] K. Uematsu, Grain-oriented microstructure of alumina ceramics made through the injection molding process, J. Amer. Cer. Soc. 80 (5) (1997) 1313–1315.
[7] P. Markondeya Raj, W.R. Cannon, Anisotropic shrinkage in tape-cast alumina: role of processing parameters and particle shape, J. Amer. Cer. Soc. 82 (10) (1999) 2619–2625.
[8] A. Shui, Z. Kato, S. Tanaka, N. Uchida, K. Uematsu, Sintering deformation caused by particle orientation in uniaxially and isostatically pressed alumina compacts, J. Eur. Cer. Soc. 22 (3) (2002) 311–316.
[9] S. Krug, J.R.G. Evans, J.H.H. ter Maat, Differential sintering in ceramic injection moulding: particle orientation effects, J. Eur. Cer. Soc. 22 (2) (2002) 173–181.
[10] A. Shui, L. Zeng, K. Uematsu, Relationship between sintering shrinkage anisotropy and particle orientation for alumina powder compacts, Scripta Mater 55 (9) (2006) 831–834.
[11] P.M. Raj, A. Odulena, W.R. Cannon, Anisotropic shrinkage during sintering of particle-oriented systems: numerical simulation and experimental studies, Acta Mater. 50 (10) (2002) 2559–2570.
[12] E.A. Olevsky, B. Kushnarev, A. Maximenko, V. Tikare, M. Braginsky, Modelling of anisotropic sintering in crystalline ceramics, Phil. Mag. 85 (19) (2005) 2123–2146.
[13] W.R. Cannon, P.M. Raj, Evolution of sintering anisotropy using a 2D finite difference method, J. Amer. Cer. Soc. 92 (7) (2009) 1391–1395.
[14] A. Vagnon, O. Lame, D. Bouvard, M.D. Michiel, D. Bellet, G. Kapelski, Deformation of steel powder compacts during sintering: correlation between macroscopic measurement and in situ microtomography analysis, Acta Mater. 54 (2) (2006) 513–522.
[15] C. Manière, G. Kerbart, C. Harnois, S. Marinel, Modeling sintering anisotropy in ceramic stereolithography of silica, Acta Mater. 182 (2020) 163–171.
[16] A. Zavaliangos, J.M. Missiaen, D. Bouvard, Anisotropy in shrinkage during sintering, Sci. Sinter. 38 (1) (2006) 13–25.
[17] F.V. DiMarcello, P.L. Key, J.C. Williams, Preferred orientation in Al2O3 substrates, J. Amer. Cer. Soc. 55 (10) (1972) 509–514.
[18] H. Watanabe, T. Kimura, T. Yamaguchi, Particle orientation during tape-casting in the fabrication of the grain-oriented bismuth titanate, J. Amer. Cer. Soc. 72 (2) (1989) 289–293.
[19] F. Kools, Factors governing the alignment of sintered anisotropic M-type ferrites, Berichte Der Deutschen Keramischen Gesellschaft 55 (6) (1978) 296–297.
[20] O.B.G. Assis, M. Ferrante, Magnetic texture enhancement densification, and grain growth in Nd-Fe-B permanent magnets, J. Mater. Synth. Process. 3 (2) (1995) 93–103.
[21] S.H. Lee, W. Lee, W.Y. Jeung, T.J. Moon, Properties of anisotropic Nd(Fe,Co)B type sintered magnets produced by powder injection moulding, Powder Metall. 41 (3) (1998) 185–188.
[22] X.K. Yuan, J. Zhu, Anisotropic distribution of phase boundaries and its potential correlation with magnetic properties in a sintered NdFeB permanent magnet, Phys. Stat. Solid. B-Basic Solid State Physics 257 (1) (2020).
[23] F. Kools, Complications in firing oriented hexaferrites due to anisotropic effects, cracking of radially oriented rings during firing, Sci. Ceram. 7 (1973) 27–44.
[24] F.J. Klug, J.S. Reed, Microstructure development during sintering of ultrafine SrO·6Fe2O3, Amer. Ceram. Soc. Bull. 57 (12) (1978) 1109–1110.

[25] P.J. McGuiness, A.J. Williams, I.R. Harris, E. Rozendaal, J. Ormerod, Sintering behavior of Ndfeb magnets, IEEE Trans. on Magnetics 25 (5) (1989) 3773–3775.
[26] F. Toussaint, D. Bouvard, P. Tenaud, E. Di Marcello, Experimental and numerical analysis of the deformation of ferrite segments during sintering, J. Mater. Proc. Tech. 147 (1) (2004) 72–78.
[27] S. Shima, M.A.E. Saleh, Compaction-induced anisotropy in internal structure of ceramic powder, J. Amer. Cer. Soc. 76 (5) (1993) 1303–1307.
[28] S. Tanaka, Y. Kuwano, K. Uematsu, Packing structure of particles in a green compact and its influence on sintering deformation, J. Amer. Cer. Soc. 90 (11) (2007) 3717–3719.
[29] A. Lichtner, D. Roussel, D. Röhrens, D. Jauffres, J. Villanova, C.L. Martin, R.K. Bordia, Anisotropic sintering behavior of freeze-cast ceramics by optical dilatometry and discrete-element simulations, Acta Mater. 155 (2018) 343–349.
[30] S. Baba, A. Maitre, N. Pradeilles, G. Antou, N. Saito, S. Tanaka, Graded evolution of anisotropic microstructure during sintering from crystal-oriented powder compact, International J. Appl. Ceram. Technol. (2019) 1–8.
[31] R.T. DeHoff, F.N. Rhines, Quantitative Microscopy, Mc Graw Hill, New York, 1968.
[32] M.M. Seabaugh, M.D. Vaudin, J.P. Cline, G.L. Messing, Comparison of texture analysis techniques for highly oriented alpha-Al2O3, J. Amer. Cer. Soc. 83 (8) (2000) 2049–2054.
[33] C. Genevois, J.M. Missiaen, F. Robaut, F. Grillon, C.P. Carry, Development of a morphological texture in relation with the crystallographic texture during sintering of strontium hexaferrites, J. Eur. Ceram. Soc. 25 (2005) 719–728.
[34] C.L. Martin, R.K. Bordia, The effect of a substrate on the sintering of constrained films, Acta Mater. 57 (2009) 549–558.
[35] C.L. Martin, et al., Evolution of defects during sintering: discrete element simulations, J. Amer. Cer. Soc. 92 (2009) 1435–1441.
[36] F. Parhami, R.M. McMeeking, A network model for initial stage sintering, Mech. Mater. 27 (1998) 111–124.
[37] D. Bouvard, R.M. McMeeking, Deformation of Interparticle necks by diffusion-controlled creep, J. Amer. Cer. Soc. 79 (3) (1996) 666–672.
[38] J. Pan, H. Le, S. Kucherenko, J.A. Yeomans, A model for the sintering of spherical particles of different sizes by solid state diffusion, Acta Mater. 46 (13) (1998) 4671–4690.
[39] R.L. Coble, Initial sintering of alumina and hematite, J. Amer. Cer. Soc. 41 (2) (1958) 55–62.
[40] C.L. Martin, R.K. Bordia, Influence of adhesion and friction on the geometry of packings of spherical particles, Phys. Rev. E 77 (2008) 31307.
[41] A. Balakrishnan, P. Pizette, C.L. Martin, S.V. Joshi, B.P. Saha, Effect of particle size in aggregated and agglomerated ceramic powders, Acta Mater. 58 (2010) 802–812.
[42] C. Eichholz, H. Nirschl, F. Chen, T.A. Hatton, DEM-simulation of the magnetic field enhanced cake filtration, AICHE J. 58 (12) (2012) 3633–3644.
[43] M. Coster, J.L. Chermant, Précis d'analyse d'images, CNRS, Paris, 1989.
[44] J.M. Chaix, F. Grillon, On the rose of directions measurements on the discrete grid of an automatic image analyser, J. Microsc. 184 (3) (1996) 208–213.
[45] X.X. Li, C. Yang, H.Z. Lu, X. Luo, Y.Y. Li, O.M. Ivasishin, Correlation between atomic diffusivity and densification mechanism during spark plasma sintering of titanium alloy powders, J. Alloys & Compounds 787 (2019) 112–122.